

Author's Accepted Manuscript

On eddy polarity distribution in the Southwestern Atlantic

Martin Saraceno, Christine Provost



www.elsevier.com/locate/dsri

PII: S0967-0637(12)00153-7
DOI: <http://dx.doi.org/10.1016/j.dsr.2012.07.005>
Reference: DSRI2127

To appear in: *Deep-Sea Research I*

Received date: 27 March 2012
Revised date: 6 July 2012
Accepted date: 11 July 2012

Cite this article as: Martin Saraceno and Christine Provost, On eddy polarity distribution in the Southwestern Atlantic, *Deep-Sea Research I*, <http://dx.doi.org/10.1016/j.dsr.2012.07.005>

This is a PDF file of an unedited manuscript that has been accepted for publication. As a service to our customers we are providing this early version of the manuscript. The manuscript will undergo copyediting, typesetting, and review of the resulting galley proof before it is published in its final citable form. Please note that during the production process errors may be discovered which could affect the content, and all legal disclaimers that apply to the journal pertain.

1 **On eddy polarity distribution in the Southwestern Atlantic**

2

3

Martin Saraceno (1) and Christine Provost (2)

4

5

(1) Centro de Investigaciones del Mar y la Atmósfera, CIMA/CONICET-UBA,
6 DCAO/FCEN-UBA, UMI-IFAECI/CNRS-CONICET-UBA, Ciudad
7 Universitaria, Pabellón II Piso 2, C1428EHA, Ciudad Autónoma de Buenos
8 Aires, Argentina.

9

10

11

(2) Laboratoire d'Océanographie et du Climat: Expérimentation et Approche
Numérique (LOCEAN), UMR 7159, Université Pierre et Marie Curie, T 45-
46, 5E, 4 place Jussieu, 75005 Paris, France.

12

13

14

Accepted manuscript

1 Abstract

2 Eddies in the Southwestern Atlantic were detected from more than 18 years of
3 satellite altimetry data using a modified version of the Okubo–Weiss method. The
4 spatial distribution and polarity of eddies were examined. A larger concentration of
5 cyclonic (anticyclonic) eddies was found on the left (right) side when looking
6 downstream on some of the largest current systems in the region, such as the South
7 Atlantic Current, the anticyclonic circulation associated with the Zapiola Drift (ZD)
8 and the northern branch of the Antarctic Circumpolar Current. In the region isolated
9 by the anticyclonic Zapiola Current, 91% of eddies were cyclonic. The observed
10 distribution of eddies is in agreement with the generation of eddies from meanders of
11 the above-mentioned currents: cyclonic (anticyclonic) eddies might detach from a
12 meander of the current on the left (right) side when looking downstream on the
13 current. Furthermore, in the ZD area, the bottom topography plays a key role in
14 determining the trajectory of eddies: the anticyclonic current associated with the ZD
15 meanders and eventually generates a cyclonic eddy that enters the ZD region only
16 across the northeastern border, where the gradient of potential vorticity is lower.
17 Finally, average surface chlorophyll-*a* concentration inside cyclonic and anticyclonic
18 eddies shows that the former have higher chlorophyll-*a* values. Thus, on average, the
19 classical eddy-pumping theory explains the difference in chlorophyll-*a* concentration
20 within eddies in the Southwestern Atlantic.

21

1 **1. Introduction**

2 Eddies are important to all aspects of oceanography and often involve the overlap of
3 research areas such as physical and biogeochemical oceanography. From a physical
4 point of view their importance resides in the fact that they play an important part in
5 the mixing processes in the surface layer of the ocean and for transporting energy, like
6 heat. Eddies can contribute significantly to the transfer of the temperature and salinity
7 characteristics of one region to another, very different, region. Thus they play an
8 important role in the meridional overturning circulation, the strength of which is a key
9 parameter for monitoring and predicting climate change [e.g. Mazloff et al., 2010;
10 Farneti et al., 2010]. From a biogeochemical point of view, cold-core (cyclonic)
11 eddies bring nutrients to the surface which become available for photosynthesis.
12 Hence they can fertilize the upper ocean to support phytoplankton blooms. Eddies
13 also play an important ecological role, since they can trap, transport and disperse
14 different communities of organisms. Thus eddies play a crucial role at regional and
15 global scales in several domains. Improving the knowledge of the spatial distribution
16 and polarity of eddies will contribute to a better understanding of their role in the
17 ocean.

18 In the Southwestern Atlantic (SWA), the eddy kinetic energy can be as high as 1700
19 $\text{cm}^2 \text{s}^{-2}$ (Figure 1). The confluence of the Malvinas Current (MC) and the Brazil
20 Current (BC) near 38°S, forms the Brazil/Malvinas Confluence region (BMC,
21 hereafter), one of the most energetic regions of the world ocean [Gordon, 1981;
22 Chelton et al., 1990]. The meanders, eddies and filaments in the BMC are
23 extraordinary in terms of their shape, size and abundance compared to other regions
24 of the ocean. High-resolution images of sea surface temperature (SST) and
25 chlorophyll-*a* concentration suggest that the associated mesoscale processes enhance
26 the productivity in the region [e.g. Barré et al., 2006; Saraceno et al., 2005].

27 The BMC is characterized by the confluence of the Subantarctic Front (SAF) and the
28 Subtropical Front (STF), which are, respectively, the northern limit of the subantarctic
29 waters and the southern limit of the subtropical waters. The region where the SAF and
30 STF merge at about 39°S is usually referred to as the Brazil/Malvinas front [e.g.
31 Saraceno et al., 2004]. A scheme of the upper circulation of the region, including the
32 position of these fronts, is shown in Figure 1. The MC is part of the northern branch
33 of the Antarctic Circumpolar Current (ACC), which carries the cold ($<7^\circ\text{C}$ at the

1 surface in winter) and relatively fresh Subantarctic Mode Water (SAMW)
2 equatorwards along the western edge of the Argentine continental shelf. The BC
3 flows polewards along the continental margin of South America as part of the western
4 boundary current of the South Atlantic subtropical gyre. It transports the warm
5 (higher than 26°C at the surface) and salty South Atlantic Central Water (SACW).
6 After its confluence with the MC, the BC separates into two branches [Peterson and
7 Stramma, 1991]. One branch turns to the north forming a recirculation cell while the
8 other branch flows southwards and returns northeastwards at about 44°S. This second
9 branch is commonly referred to as the overshoot of the Brazil Current and, east of
10 45°W, it forms the South Atlantic Current [Peterson and Stramma, 1991]. After the
11 collision with the BC, the main flow of the MC describes a sharp loop forming the
12 Malvinas return flow. The Malvinas return flow flows southwards and turns eastwards
13 at 49°S.

14 Further towards the center of the South Atlantic, an important feature that affects the
15 large-scale circulation is the presence of a large zonal sedimentary deposit known as
16 the Zapiola Drift (ZD). The effect of this submarine feature on the surface of the
17 ocean is clearly observed in the satellite images of SST, SST gradient, chlorophyll-*a*
18 and sea surface height (SSH) [Saraceno et al., 2005]. The anticyclonic circulation
19 around the ZD is eddy-driven [Dewar, 1998]. A meridional transport of 80 Sverdrups
20 ($1 \text{ Sverdrup} = 10^6 \text{ m}^3 \text{ s}^{-1}$) on the western and eastern flanks of the ZD with southgoing
21 and northgoing currents, respectively, of about equal magnitude, has been estimated
22 from in situ measurements during the WOCE A11 cruise [Saunders and King, 1995b].
23 Satellite altimetry data [Saraceno et al., 2009] and model outputs [Bigorre and Dewar,
24 2009; Venaille et al., 2011] suggest that the anticyclonic circulation associated with
25 the ZD is characterized by an important interannual variability. Despite the
26 importance of eddies in the ZD circulation, a precise description of the interaction
27 between eddies and the anticyclonic circulation has not been provided yet.

28 Eddies have been detected in the Southwestern Atlantic since the first global satellite
29 infrared images of SST were acquired [Legeckis and Gordon, 1982]. Despite their
30 high spatial resolution, sea surface temperature (SST) images are limited by the cloud
31 coverage. In contrast, satellite radar altimetry sensors provide “cloud-free” SSH
32 images. Using a combination of along-track SSH, climatological temperature and
33 salinity fields, Lentini et al. [2006] showed that 40 warm-core eddies were released by
34 the BC in the period 1993-1998. Analysis of gridded SSH maps suggested that a

1 much larger number of eddies is present in the region [Saraceno, 2010]. Mesoscale
2 surface circulation can be accurately estimated from SSH data when two or more
3 satellite missions are used to construct gridded fields [Pascual et al., 2006; Chelton et
4 al., 2011a]. Thus, gridded maps of SSH data are particularly useful in the study of
5 mesoscale structures and of the interaction between mean currents and eddies in the
6 ocean. Several studies have therefore used satellite SSH data to detect and track
7 eddies in the ocean [e.g. Chaigneau et al., 2008; Chaigneau et al., 2009; Chelton et al.,
8 2011a].

9 We took advantage of the 18-year-long altimetry time-series to detect eddies and track
10 them in the Southwestern Atlantic. We used one of the most popular techniques to
11 detect eddies, the Okubo–Weiss (OW) algorithm [Okubo, 1970; Weiss, 1991; Isern-
12 Fontanet et al., 2003]. The OW algorithm is based on physical criteria, whereas other
13 methods of eddy detection are more geometrical. Because of the complex nature of
14 the flow field in the Southwestern Atlantic and in order to distinguish eddies from
15 meanders we had to modify the OW method slightly. We validated the modified
16 method and then applied it to the whole altimetry time-series. We examined the
17 distribution of eddies and of eddy polarity and discuss their relation with the
18 circulation in the region.

19 The article is organized as follows. Section 2 provides a brief description of the
20 datasets. The methodology and the validation strategy are explained in section 3.
21 Section 4 presents and discusses the results. Section 5 summarizes the results and
22 outlines perspectives.

23

1 **2. Data**

2

3 2.1 Satellite sea-level anomaly

4 We used the reference, delayed time-series of the gridded data fields of sea level
5 anomaly (SLA) produced by Ssalto/Duacs and distributed by AVISO
6 (www.aviso.oceanobs.com). SLA AVISO fields are computed with reference to a
7 mean for the period 1993–1999. We extracted the gridded data fields of SLA for the
8 region of interest (60°W–35°W, 50°S–35°S) from the global SLA fields for the period
9 14 October 1992–1 December 2010 (18+ years).

10 Satellite altimetry missions have accurately determined sea surface height (SSH) since
11 the launch of the TOPEX/Poseidon (T/P) satellite in 1992 [Fu and Cazenave, 2001].
12 Six satellite altimetry missions (Jason-1, ERS-1, ERS-2, Envisat, GFO and Jason-2)
13 have been launched since then. The processing of along-track data from the altimetric
14 missions into gridded fields of SSH was described by Le Traon et al. [2003]. The
15 reference time-series always uses two contemporary satellite missions to construct the
16 interpolated SSH fields: one in a 10-day repeat orbit (T/P, followed by Jason-1 and
17 Jason-2) and another one in a 35-day repeat orbit (ERS-1, followed by ERS-2 and
18 Envisat). The time-series is produced weekly on a $1/3^\circ \times 1/3^\circ$ grid in a Mercator
19 projection. The objective procedure to obtain the gridded fields of SSH by AVISO
20 includes a spatial filtering that has half-power filter cut-off wavelengths of about 2° in
21 latitude and 2° in longitude, which corresponds to an e-folding radius of about 0.4° , or
22 about 40 km at mid-latitudes [Chelton et al., 2011a]. The dataset can then be used to
23 detect eddies whose radii are larger than 40 km. We only considered eddies detected
24 offshore in depths greater than 200 m. Indeed, intrinsic difficulties affect the
25 corrections applied to the altimeter data on the Patagonian shelf (e.g. wet tropospheric
26 component, tidal component) and data are usually flagged as unreliable within a
27 certain distance of the coast. Moreover, the interpolation of along-track data provides
28 only marginal resolution of high-frequency and small-scale structures which are
29 abundant on the Patagonian shelf [Acha et al., 2004].

30

31 2.2 SeaWiFS-derived chlorophyll-*a* concentrations

32 Near-surface chlorophyll-*a* concentrations used in this study consist of 8-day, 9-km
33 gridded estimates derived from satellite measurements of ocean color by the Sea-

1 viewing Wide Field-of-view Sensor (SeaWiFS) [McClain et al., 1998] using the
2 Garver–Siegel–Maritorena (GSM) semi-analytical ocean color algorithm [Garver and
3 Siegel, 1997; Maritorena et al., 2002]. These chlorophyll-*a* concentration fields are
4 available online at
5 <ftp://ftp.oceancolor.ucsb.edu/pub/org/oceancolor/MEaSURES/Seawifs/>. Despite the
6 fact that cloud cover places a strong limitation on this dataset, the composite average
7 minimizes the cloud-cover problem and keeps a reasonable time resolution to allow
8 detection of mesoscale features in the ocean surface layer. Color images are used in
9 the validation strategy described in Section 3.3 and to composite chlorophyll-*a*
10 concentrations within eddies of the same polarity. The most common explanation for
11 the different chlorophyll-*a* concentration in the eddy interior is that the geostrophic
12 adjustment required to maintain the circulation implies a thermocline rise inside the
13 cyclonic eddies and a depression in the anticyclonic eddy. When the nutricline and the
14 thermocline are coincident, then enhanced production is expected within cyclonic
15 eddies. However this simple explanation has its shortcomings: complex non-linear
16 biophysical dynamics control the phytoplankton growth, which depends on the critical
17 balance of stirring, mixed-layer depth, stability of the water column, temperature and
18 availability of light.

19

20 2.3 Surface-buoy trajectories

21 Satellite-tracked drifter data used in this work are part of the global data set available
22 from the Drifter Data Assembly Center (DAC) at the National Oceanographic and
23 Atmospheric Administration's Atlantic Oceanographic and Meteorological Laboratory
24 (NOAA/AOML). The data set is public and can be downloaded from AOML's ftp
25 server (<ftp://ftp.aoml.noaa.gov/phod/pub/buoydata>).

26 Quality control at DAC involves the interpolation of the raw fixes (16 to 20 satellite
27 fixes per day per drifter) uniformly at six-hour intervals using a kriging interpolation
28 scheme [Hansen and Poulain, 1996]. The data from drifters with no drogue attached
29 were discarded, as were all interpolated positions with an uncertainty greater than 1
30 km. The remaining trajectories were low-pass-filtered with a 2-day Gaussian filter in
31 order to remove tidal fluctuations and other high-frequency variability of no interest
32 in the present study. The Ekman component, estimated following Ralph and Niiler

4 [1999], was excluded: in the region under consideration, the estimated Ekman
 5 velocity is similar to the velocity uncertainty (less than 1 cm s^{-1} , even with strong
 6 winds).

5

6 3. Methodology

7 3.1 Eddy-detection

9 The Okubo–Weiss method may be summarized as follows. First, surface velocities
 10 are estimated from SLA following the geostrophic approximation:

$$v = \frac{g}{f} \frac{\partial \eta}{\partial x} \quad (1) \quad u = -\frac{g}{f} \frac{\partial \eta}{\partial y} \quad (2)$$

10

14 where u and v are, respectively, the zonal and meridional geostrophic surface velocity
 15 components, η is SLA, g is the gravity and f is the Coriolis factor. The relative
 16 vorticity (ω), normal strain (S_n) and shear strain (S_s) deformation rates can then be
 17 computed:

$$\omega = v_x - u_y \quad (3) \quad S_n = u_x - v_y \quad (4) \quad S_s = v_x + u_y \quad (5)$$

15

16 The Okubo–Weiss parameter (W) can be then computed as:

$$W = S_n^2 + S_s^2 - \omega^2 \quad (6)$$

17

22 W was developed first by Okubo [1970] and later by Weiss [1991]; the automatization
 23 of the method was first implemented by Isern-Fontanet et al. [2003]. The method
 24 identifies regions of the flow where the relative vorticity component dominates the
 25 strain tensors, defined as the center of the eddy. Considering horizontally non-
 26 divergent flows, i.e. where $u_x + v_y = 0$, equation 6 simplifies to:

$$W = 4(v_x u_y + u_x^2) \quad (7)$$

23

26 Eddies are identified as the regions where $W < b\sigma$, σ being the standard deviation of
 27 the geostrophic velocity field at each time, b being a constant value. We used a value
 28 for b that has been successfully used in several regions: 0.2 [Chaigneau et al., 2008].

1 Results (not shown) obtained with the classical OW algorithm described above
 2 indicated that several eddies were identified in regions where non-closed contours of
 3 SLA were present. This happens in regions where a strong curvature of the
 4 geostrophic velocities exists; i.e. where strong meanders are present. The
 5 Brazil/Malvinas Confluence and overshoot regions are the two regions where most of
 6 the eddies corresponding to non-closed contours were detected. To overcome this
 7 difficulty we adopted the following strategy: Once we obtained the center of the eddy
 8 by applying the OW algorithm described above, we looked for the corresponding
 9 SLA value and searched for the highest (lowest) closed contour for cyclonic
 10 (anticyclonic) eddies. The center of the eddy was then re-estimated based on the new
 11 contour. We stopped the algorithm when one of the following two conditions first
 12 arose: (i) the length of the eddy contour was larger than the previous one by more than
 13 7 pixels; (ii) the distance between any pair of points within the contour considered
 14 must be less than 400 km. These two conditions avoid cases of multiple centers and
 15 preserve the usual notion of a compact form for rotating vortices. The second
 16 condition is the same as in Chelton et al. [2011a]. We then estimated the amplitude of
 17 each eddy as the absolute difference between the SLA at the center of the eddy and
 18 the average of the SLA at the corresponding contour. We considered only eddies with
 19 amplitudes greater than 2 cm. The 2-cm threshold was chosen after a sensitivity study
 20 (section 3.3).

21 The simple technique described above combines the physical criteria of the OW
 22 method with the conventional geometric definition of an eddy as a closed contour of
 23 SLA.

24 3.2 Eddy tracking

25 The eddy-tracking algorithm was adapted from Penven et al. [2005] and follows the
 26 approach used by Chaigneau et al. [2008]. The method minimizes a distance D
 27 between the detected eddies of two consecutive maps. For each eddy (e_1) identified
 28 on a given map at time t_1 and for each eddy (e_2) identified on the next map at time t_2
 29 and rotating in the same sense as e_1 , the non-dimensional distance $D_{e_1;e_2}$ is defined as:

$$30 \quad D_{e_1;e_2} = \sqrt{\left(\frac{\Delta D}{D_0}\right)^2 + \left(\frac{\Delta R}{R_0}\right)^2 + \left(\frac{\Delta \mu}{\mu_0}\right)^2 + \left(\frac{\Delta EKE}{EKE_0}\right)^2} \quad (8)$$

31

1 where ΔD is the spatial distance between e1 and e2, and ΔR , $\Delta \mu$ and ΔEKE are,
2 respectively, the radius, the vorticity and the eddy kinetic energy (EKE) differences
3 between e1 and e2. D_0 , R_0 , μ_0 and EKE_0 are, respectively, the characteristic length
4 scale ($D_0 = 100$ km), the characteristic radius ($R_0 = 50$ km), the characteristic vorticity
5 ($\mu_0 = 10^{-6} \text{ s}^{-1}$) and the characteristic EKE ($EKE_0 = 100 \text{ cm}^2 \text{ s}^{-2}$). $D_{e1:e2}$ represents the
6 degree of similarity between two eddies (the smaller the value, the higher the
7 similarity between e1 and e2). Thus, the algorithm selects the eddy pair (e1, e2) that
8 minimizes $D_{e1:e2}$ and considers this pair to be the same eddy that is tracked from t1 to
9 t2. To avoid jumping from one track to another, the search distance, ΔD , was
10 restricted to 150 km. Eddies may also disappear between consecutive maps,
11 particularly if they pass into the gaps between satellite ground tracks. To minimize
12 this problem, we searched for the same eddy for two weeks after its disappearance.

13 3.3 Validation strategy

14 To determine the accuracy of the methodology described above we applied an
15 objective validation protocol similar to the one described by Chaigneau et al. [2008].
16 The location and number of eddies detected with the modified OW method were
17 compared with the location and number of eddies detected by two different methods,
18 one using drifting buoys (method A1), the other using composite images of
19 chlorophyll-*a* concentration and SLA (method B1). The two methods are described
20 below. An example illustrating eddies detected by the three methods (modified OW,
21 A1 and B1) is shown in Figure 2.

22 3.3.1 Method A1: eddy detection using drifting buoys

23 We selected buoy trajectories that clearly showed loops suggesting eddy-trapping,
24 that is trajectories that made more than two complete loops (clockwise or
25 anticlockwise) in a geographical region no larger than 3° by 3° . This way, fifty-two
26 trajectories were selected. For each section of the trajectory considered as
27 corresponding to an eddy, the center and radius were computed taking into account
28 the positions of the buoy in the region where the buoy made at least two complete
29 loops. The center was estimated as the intersection of the average latitude and
30 longitude of the selected buoy positions. The radius was estimated as half of the
31 largest distance between positions.

1 3.3.2 Method B1: eddy detection using images of chlorophyll-*a* concentration and
2 SLA

3 Ten randomly selected maps of SLA were used in combination with the
4 corresponding chlorophyll-*a* concentration images. An example is shown in Figure 2.
5 We chose the center and radius of each vortex present in the ten composite images by
6 a careful inspection of the closed contours of SLA and the spatial distribution of
7 chlorophyll-*a* concentration. Each composite image was displayed in a PC screen and
8 using an interactive program we selected the center and radius of each eddy. We
9 repeated the procedure separately for cyclonic and anticyclonic eddies.

10 3.3.3 Comparison strategy

11 To quantify the differences between the number of eddies detected by methods A1
12 and B1 with those detected by the modified OW method, we computed, for the
13 cyclonic and anticyclonic eddies separately, the intersection and complementary areas
14 of each eddy. If the intersection area was larger than 50% of the complementary area,
15 we considered the eddy detection to be correct. A sensitivity study (results not shown)
16 in which we modified the radius and position of two overlapping eddies showed us
17 that the 50% value is a good choice for the correct detection of eddies whose radii do
18 not differ by more than 50% and for which the distance between the centers is shorter
19 than the average of the two eddies' radii.

20 While method A1 could only be used to compare 52 eddies, we counted a total of 223
21 eddies in the 10 images selected at random (method B1). Results are presented in
22 Section 4.1.

23

24 **4. Results**

25 4.1 Validation

26 As discussed in the data section (2.1), we do not consider the continental platform.
27 The total number of eddies detected by each method (A1, B1, OW) and their polarity,
28 whether cyclonic or anticyclonic, are reported in Table 1.

29 According to the criteria defined in section 3.3.3, of the 52 eddies detected using
30 method A1 (drifting buoys), 42 matched those detected by the OW method, leading to
31 a 81% agreement between the A1 and OW methods.

1 The B1 method (composite color images and SLA maps) and the OW method
2 detected 223 and 264 eddies, respectively, in the 10 randomly selected images that
3 lead to an agreement of 80% between the A1 and OW methods. Inspection of the 41
4 mismatched eddies showed that they were randomly distributed and equally
5 proportioned between cyclonic and anticyclonic ones. On the other hand, methods B1
6 and OW both gave a slightly larger number of cyclonic than anticyclonic eddies
7 (Table 1).

8 Thus, the comparison of the OW method with methods A1 and B1 suggests that the
9 uncertainty associated with the automated eddy-detection methodology used in this
10 work is less than 20%. Detecting eddies with amplitudes smaller than 2 cm led to
11 larger differences between the methods, so we kept the 2-cm threshold, which
12 corresponds to the accuracy of SLA maps. We consider that the modified OW method
13 is validated and applied it to the entire altimetric time series.

14

15 4.2 Eddy distribution

16 Figure 3 shows the distribution of cyclonic (C) and anticyclonic (A) eddies in the
17 Southwestern Atlantic. First, there are more C than A eddies inside the area defined
18 by the ZD. In the rectangular box contained inside the longest potential vorticity
19 contour that encloses the ZD (see Figure 3), the number of C eddies is 10 times
20 greater than the number of A eddies (182 and 18, respectively, for the period
21 considered). On the other hand, just outside the ZD, the number of A eddies (236) is
22 greater than the number of C eddies (180). The region defined as outside the ZD was
23 estimated as a one-degree margin that follows the closed potential vorticity contour
24 depicted in Figure 3. The two results described above are compatible with the
25 following explanation, schematically shown in Figure 4. The ZD is a dynamically
26 isolated region [Dewar, 1998; Saraceno et al., 2005, 2009] which is contoured by an
27 A circulation. We propose that eddies that can enter the ZD isolated area are
28 detachments attributable to meanders in the A circulation associated with the ZD
29 (Figure 4). This mechanism may also explain why the number of A eddies is higher
30 than the number of C eddies just outside the ZD area. The eddy-formation mechanism
31 is the same as that used to explain the formation of A (C) eddies north (south) of the
32 Gulf Stream in the North Atlantic [e.g. Schmitz and Holland, 1982].

1 Second, as expected, the number of eddies is maximum in regions where the EKE is
2 higher, such as the BMC region or the region between the SAF and the ZD, south of
3 46°S (Figure 1 and Figure 3). C eddies are more numerous north of the STF, while A
4 eddies are more numerous along or south of the STF (Figure 3). Meanders of the BC
5 and the consequent generation of A (C) eddies south (north) of the mean position of
6 the STF is a potential mechanism explaining the distribution of eddies in the BMC
7 region. Detachments of eddies from meanders of the Antarctic Circumpolar Current
8 (ACC), which flows westwards along the SAF, may also explain the larger
9 concentration of C eddies north of the SAF between 50°W and 35°W (Figure 3).
10 However, a larger concentration of A eddies south of the SAF is not observed. Two
11 spots centered approximately at 50°S, 48°W and 50°S, 37°W with a significant
12 number of eddies (both C and A) are located south of the SAF and correspond to
13 regions where the sea floor is shallower than it is in the surrounding regions,
14 enhancing the formation of meanders and eddies. This is also reflected by large values
15 of EKE (Figure 1).

16 Third, eddies are mostly observed within the region with potential vorticity larger
17 than $-2.1 \times 10^{-8} \text{ m}^{-1} \text{ s}^{-1}$ (Figure 3). Indeed, the $-2.1 \times 10^{-8} \text{ m}^{-1} \text{ s}^{-1}$ potential vorticity
18 contour appears as a barrier for eddies except for the two locations south of the SAF
19 mentioned above and for the region north of Brazil/Malvinas front. The modified OW
20 algorithm did not find eddies either in the MC itself or in the Malvinas return-flow
21 area. Evidently, the Brazil/Malvinas front is a barrier for eddies. The position of the
22 Brazil/Malvinas front, indicated in Figure 3, has been estimated from infrared sea
23 surface temperature images [Saraceno et al., 2004], hence a completely independent
24 dataset.

25 Fourth, there is a local maximum in the number of C eddies centered just over the top
26 of the ZD; that is, where the ZD reaches its maximum height (see Figure 3 at 44.5°W,
27 45.5°S). This can be explained by considering that, once C eddies are generated inside
28 the ZD area, the bottom topography favors their location over the top of the ZD:
29 assuming that bottom friction is weak, the conservation of potential vorticity implies
30 that a vorticity anomaly travelling upslope would need to decrease its relative
31 vorticity (neglecting the *beta* effect for simplicity), so that anticyclones would
32 weaken, whereas cyclones would be reinforced on their way towards the peak of the
33 ZD.

1 Finally, comparison of potential vorticity contours (Figure 5) with the trajectories of
2 the C and A eddies that we could follow for more than 6 weeks (Figure 6) also
3 suggests a relevant observation: most of the C eddies that enter the ZD region did so
4 from the northeastern flank. This is the region where the slope of the potential
5 vorticity contours is less pronounced (Figure 6). It is therefore more likely that the A
6 current associated with the ZD is able to meander more vigorously in this region or, in
7 other words, is less controlled by the topographic gradient that defines the ZD. As a
8 consequence, C eddies generated as illustrated in Figure 4 enter the ZD area more
9 frequently on the northeastern flank of the ZD region.

10

11 4.3 Temporal evolution of cyclonic eddies inside the Zapiola Drift area

12 The time-series of the number of C eddies inside the ZD area suggests that eddies
13 entered at specific dates (Figure 7). The time-series is compared with an estimation of
14 the transport around the ZD (Figure 7). Using satellite altimetry data for the period
15 1993–2006, Saraceno et al. [2009] showed that the 4-year low-pass-filtered transport
16 time-series associated with the ZD had a local minimum during the years 1998–2003.
17 We extended the transport estimation to compare it with the time-series of the number
18 of C eddies that enter the ZD area produced in this work (Figure 7). The comparison
19 suggests that when the low-frequency component of the transport associated with the
20 ZD is less than 25 Sverdrups, more eddies are able to enter the ZD area and, when the
21 transport is larger than 25 Sverdrups, fewer C eddies enter the ZD area. On the other
22 hand, the non-filtered transport time-series (not shown) does not significantly
23 correlate at any time lag with the number of C eddies inside the ZD area. While the
24 low-frequency transport may affect the distribution of eddies, an instantaneous
25 response is not necessarily expected. In other words, the foregoing results suggest that
26 the low-frequency component of the transport of the anticyclonic current associated
27 with the ZD may be associated with the number of C eddies inside the ZD area,
28 whereas this is not observed at higher frequencies.

29 The yearly average temporal distribution of A eddies that entered the ZD area (18 in
30 total) shows that a maximum of three eddies per year entered during the years 2003
31 and 2007, whereas during the other years a maximum of two eddies per year entered
32 (not shown). The low number of A eddies does not allow any robust statistical

1 analysis. Furthermore, trajectories of long-lived eddies (Figure 6) suggest that A
2 eddies that entered the ZD area dissipated very quickly.

3

4 **5. Summary and discussion**

5 Eddies in the Southwestern Atlantic are detected from satellite altimetry data using a
6 modified version of the OW method. Distribution of eddies in the region shows two
7 salient observations: (i) the number of C eddies detected inside the ZD area is ten
8 times larger than the number of A eddies; and (ii) a larger number of A eddies were
9 detected just outside the ZD area. We proposed that perturbations of the A circulation
10 associated with the ZD may generate meanders which, when occurring inside the ZD
11 area, could detach from the main current and generate a C eddy (Figure 4). A similar
12 mechanism may explain the higher number of A eddies observed outside the ZD area.

13 The absence of A eddies inside the ZD anticyclone is a strong indication that
14 meandering is occurring. Although very few anticyclonic eddies made their way to
15 the center of the ZD region, this happened when the associated circulation was at its
16 weakest (Figure 7) and indicates the key role of the mean anticyclonic Zapiola
17 Current in selecting what type of eddies can enter the ZD anticyclone.

18 However, another explanation for a preference for cyclonic eddies near the ZD is
19 linked to the conservation of potential vorticity, assuming that bottom friction is
20 weak. Indeed a vorticity anomaly traveling upslope would need to decrease its relative
21 vorticity, so that anticyclonic eddies would weaken, whereas cyclonic eddies would
22 be reinforced on their way towards the ZD center. Figure 6 supports this mechanism,
23 since it shows that anticyclones quickly disappear after entering the ZD area.

24 The preferred path for C eddies to enter the ZD area is the northeastern side of the
25 region, where the potential vorticity gradient is lower compared to other sides (Figure
26 5). Thus, the distribution of eddies described in this work is coherent with an
27 anticyclonic ZD circulation that might meander and release more eddies on the
28 northeastern side of the region.

29 As the elevation of the ZD results in a selection mechanism to filter A eddies, we
30 could anticipate that a similar result should occur in other places with similar
31 characteristics. In the North Atlantic, the Azores Plateau (AP) is an anomaly of the

1 Mid-Atlantic Ridge (MAR), located approximately at 40°N, 30°W. The AP appears as
2 a local topographic elevation of roughly 1200 m altitude relative to the MAR, and a
3 lateral extent of 1500 km in both the meridional and zonal directions, and therefore
4 with similar characteristics to the ZD. Evidence also exists that there is an
5 anticyclonic gyre over the AP [Klein and Siedler, 1989; Pollard et al, 1996], but of
6 one to two orders of magnitude lower intensity in transport compared to the
7 anticyclonic ZD Current (100 Sv, according to Saunders and King [1995a]). Since we
8 do not estimate eddies in the AP region, we compared eddy censuses in both the ZD
9 and AP regions by looking at figures from Chelton et al. [2011a]. Their figures 4a and
10 8 clearly show that more cyclonic than anticyclonic eddies entered the ZD region, as
11 we illustrated in the present article. A white spot coincident with the AP region is
12 visible in their Figure 4a [Chelton et al., 2011a], clearly suggesting the bathymetric
13 forcing. However, no predominance of a given eddy polarity is observed in the AP
14 region (their Figure 8). This may be due to the difference in strength of the two
15 anticyclonic currents associated with the seabed elevations.

16 The prospects for continuing the work presented here include a study of the
17 contribution of eddies to an explanation of the spatio-temporal distribution of
18 chlorophyll-*a* in the Southwestern Atlantic. As a preliminary result, Figure 8 shows
19 that the average surface chlorophyll-*a* concentration in C eddies is higher than that in
20 A eddies. Thus, on average, the classical eddy pumping theory, i.e. uplift of the upper
21 thermocline inside the eddy to bring nutrients into the euphotic zone [e.g.
22 McGillicuddy et al., 1998; Siegel et al., 1999], explains the difference in chlorophyll-
23 *a* concentration in the two types of eddies in the SWA. However, careful inspection of
24 the different mechanisms (e.g. eddy pumping, eddy advection, wind-forced Ekman
25 pumping and submesoscale effects) that might explain the spatio-temporal
26 distribution of the chlorophyll-*a* concentration forced by the eddies is necessary
27 before assessing which mechanism makes the largest contribution. Given the wide
28 range of eddy energy (e.g. 10^2 to $2 \times 10^3 \text{ cm}^2 \text{ s}^{-2}$) and the sharp contrasts in
29 chlorophyll-*a* concentration (0.05 to 10 mg m^{-3}), the SWA is a useful region to test
30 the role of eddies in the chlorophyll-*a* distribution in different environments.

31

32

1

2 Acknowledgments:

3 The altimeter products were produced by Ssalto/Duacs and distributed by AVISO,
4 with support from CNES (<http://www.aviso.oceanobs.com/duacs/>). U. Zajaczkovski
5 helped with the selection of the drifter data. D. Oks contributed to the computation of
6 data for Figure 8. This work is a contribution to projects ANPCyT PICT 2009-27, IAI
7 CRN2076, CONICET PIP 112-200801-03072 and UBACYT 2008 X176. CNES
8 support is acknowledged. We warmly thank Ray Griffiths for his most valuable
9 comments on the manuscript.

10

11

12

13

Accepted manuscript

1 References

- 2 **Acha**, E. M., H. W. Mianzan, R. A. Guerrero, M. Favero, J. Bava, 2004. Marine
3 fronts at the continental shelves of austral South America - Physical and ecological
4 processes, *J. Mar. Syst.*, 44, 83-105.
- 5 **Barré**, N., C. Provost, M. Saraceno, 2006. Spatial and temporal scales of the Brazil
6 Malvinas Current confluence documented by simultaneous MODIS Aqua 1.1-km
7 resolution SST and color images. *Adv. Space Res.*, 37, 770-786.
- 8 **Bigorre**, S. and W.K. Dewar, 2009. Oceanic time variability near a large scale
9 topographic circulation. *Ocean Modelling*, 29(3), 176-188.
- 10 **Chaigneau**, A., A. Gizolme, C. Grados, 2008. Mesoscale eddies off Peru in altimeter
11 records: identification algorithms and eddy spatio-temporal patterns. *Prog.*
12 *Oceanogr.*, 79(2-4), 106-119.
- 13 **Chaigneau**, A., G. Eldin, B. Dewitte, 2009. Eddy activity in the four major upwelling
14 systems from satellite altimetry (1992-2007). *Prog. Oceanogr.*, 83(1-4), 117-123.
- 15 **Chelton**, D.B., M.G. Schlax, R.M. Samelson, 2011a. Global observations of
16 nonlinear mesoscale eddies. *Prog. Oceanogr.*, 91(2), 167-216.
- 17 **Chelton**, D.B., M.G. Schlax, D.L. Witter, J.G. Richman, 1990. Geosat altimeter
18 observations of the surface circulation of the Southern Ocean. *J. Geophys. Res.*,
19 95(C10), 17,877-17,903.
- 20 **Dewar**, W.K., 1998. Topography and barotropic transport control by bottom friction.
21 *J. Mar. Res.*, 56(2), 295-328.
- 22 **Farneti**, R., T.L. Delworth, A.J. Rosati, S.M. Griffies, Fanrong Zeng, 2010. The role
23 of mesoscale eddies in the rectification of the Southern Ocean response to climate
24 change. *J. Phys. Oceanogr.*, 40, 1539-1557. doi: 10.1175/2010JPO4353.1
- 25 **Fu**, L.L. and A. Cazenave, 2001. *Satellite Altimetry and the Earth Sciences: A*
26 *Handbook of Techniques and Applications*, Academic Press, San Diego, Calif. 463pp.
- 27 **Garver**, S.A. and D.A. Siegel, 1997. Inherent optical property inversion of ocean
28 color spectra and its biogeochemical interpretation: 1. Time series from the Sargasso
29 Sea. *J. Geophys. Res.*, 102, 18,607-18,625.
- 30 **Gordon**, A.L., 1981. South Atlantic thermocline ventilation. *Deep-Sea Res. Part A.*
31 *Oceanographic Research Papers*, 28(11), 1239-1264.
- 32 **Legeckis**, R. and A. L. Gordon, 1982. Satellite Observations of the Brazil and
33 Falkland Currents - 1975 to 1976 and 1978, *Deep-Sea Res. Part A -Oceanographic*
34 *Research Papers*, 29(3), 375-401.
- 35 **Lentini** A. D., G. J. Goni, D. B. Olson, 2006. Investigation of Brazil Current rings in
36 the confluence region. *J. Geophys. Res.*, 111, C06013, doi:10.1029/2005JC002988.
- 37 **Hansen**, D. V. and P.-M. Poulain, 1996. Quality control and interpolations of WOCE-
38 TOGA drifter data. *J. Atmos. Oceanic Technol.*, 13, 900-909.
- 39 **Isern-Fontanet**, J., E. García-Ladona, J. Font, 2003. Identification of marine eddies
40 from altimetry. *J. Atmos. Oceanic Technol.*, 20, 772-778.
- 41 **Klein**, B. and G. Seidler, 1989. On the origin of the Azores Current. *J. Geophys. Res.*,
42 94, 6159-6168.

- 1 **Le Traon**, P.Y., Y. Faugere, F. Hernandez, J. Dorandeu, F. Mertz, M. Ablain, 2003.
2 Can we merge GEOSAT follow-on with TOPEX/Poseidon and ERS-2 for an
3 improved description of the ocean circulation? *J. Atmos. Oceanic Technol.* 20, 889-
4 895.
- 5 **Maritoren**a, S., D. A. Siegel, A. Peterson, 2002. Optimization of a semi-analytical
6 ocean color model for global scale applications. *Rem. Sens. Environ.*, 94, 429-440.
- 7 **Mazloff**, M. R., P. Heinback, C. Wunsch, 2010: An eddy-permitting Southern Ocean
8 state estimate. *J. Phys. Oceanogr.*, 40, 880-899.
- 9 **McClain**, C.R., M. L. Cleave, G. C. Fledman, W. W. Gregg, S. B. Hooker, N. Kurig,
10 1998. Science quality SeaWiFS data for global biosphere research. *Sea Technol.*, 39,
11 10-16.
- 12 **McGillicuddy**, D. J., Jr., A. R. Robinson, D. A. Siegel, H. W. Jannasch, R. Johnson,
13 T. D. Dickey, J. McNeil, A. F. Michaels, A. H. Knap, 1998. Influence of mesoscale
14 eddies on new production in the Sargasso Sea. *Nature*, 394, 263-266,
15 doi:10.1038/28367.
- 16 **Okubo**, A., 1970. Horizontal dispersion of floatable particles in the vicinity of
17 velocity singularities such as convergences. *Deep-Sea Res.* 17, 445-454.
- 18 **Penven**, P., V. Echevin, J. Pasapera, F. Colas, J. Tam, 2005. Average circulation,
19 seasonal cycle, and mesoscale dynamics of the Peru Current system: a modeling
20 approach. *J. Geophys. Res.*, Oceans, 110, C10021. doi:10.1029/2005JC002945.
- 21 **Pollard**, R., M. Griffiths, S. Cunningham, J. Read, F. Perez, A. Rios, 1996. Vivaldi,
22 1991: a study of the formation, circulation and ventilation of Eastern North Atlantic
23 Central Water. *Prog. Oceanogr.*, 37, 167-192.
- 24 **Pascual**, A., Y. Faugere, G. Larnicol, P.-Y. Le Traon, 2006. Improved description of
25 the ocean mesoscale variability by combining four satellite altimeters. *Geophys. Res.*
26 *Lett.*, 33, 02611.
- 27 **Peterson**, R.G. and L. Stramma, 1991. Upper-level circulation in the South Atlantic
28 Ocean. *Prog. Oceanogr.*, 26(1), 1-73.
- 29 **Ralph**, E. A. and P. P. Niiler, 1999. Wind-driven currents in the tropical Pacific. *J.*
30 *Phys. Oceanogr.*, 29(9), 2121-2129.
- 31 **Saraceno**, M., C. Provost, A. R. Piola, J. Bava, A. Gagliardini, 2004. Brazil Malvinas
32 Frontal System as seen from 9 years of advanced very high resolution radiometer
33 data. *J. Geophys. Res.*, 109, C05027.
- 34 **Saraceno**, M., C. Provost, A. R. Piola, 2005. On the relationship between satellite-
35 retrieved surface temperature fronts and chlorophyll-*a* in the western South Atlantic.
36 *J. Geophys. Res.*, C: Oceans, 110(11), 1-16.
- 37 **Saraceno**, M., C. Provost, U. Zajaczkovski, 2009. Long-term variation in the
38 anticyclonic ocean circulation over the Zapiola Rise as observed by satellite altimetry:
39 evidence of possible collapses. *Deep-Sea Res. Part I: Oceanographic Research*
40 *Papers*, 56(7), 1077-1092.
- 41 **Saraceno**, M., 2010. Mesoscale variability in the Brazil/Malvinas Confluence region
42 revisited. *EOS Trans. AGU*, 91(26), *Meet. Am. Suppl.*, Abstract 851231.

- 1 **Siegel**, D. A., E. Fields, D. J. McGillicuddy Jr., 1999. Mesoscale motions, satellite
2 altimetry and new production in the Sargasso Sea. *J. Geophys. Res.*, 104, 13,359-
3 13,379, doi:10.1029/1999JC900051.
- 4 **Saunders**, P. and B. A. King, 1995a. Bottom current derived from a shipborne ADCP
5 on WOCE cruise A11 in the South Atlantic. *J. Phys. Oceanogr.* 25, 329-347.
- 6 **Saunders**, P. M. and B. A. King, 1995b. Oceanic fluxes on the WOCE A11 Section.
7 *J. Phys. Oceanogr.*, 25(9), 1942-1958.
- 8 **Schmitz**, W. J. and W. R. Holland, 1982. A preliminary comparison of selected
9 numerical eddy-resolving general-circulation experiments with observations. *J. Mar.*
10 *Res.*, 40(1), 75 -117.
- 11 **Venaille**, A., J. Le Sommer, J.-M. Molines, B. Barnier, 2011. Stochastic variability of
12 oceanic flows above topography anomalies. *Geophys. Res. Lett.*, 38, L16611,
13 doi:10.1029/2011GL048401.
- 14 **Weiss**, J., 1991. The dynamics of enstrophy transfer in two-dimensional
15 hydrodynamics. *Physica*, D 48, 273-294.
- 16
17
18
19

1 Tables

2

3

Method	Cyclonic	Anticyclonic	Total
A1	23	29	52
B1	118	105	223
OW	137	127	264

4

5 Table 1: Cyclonic, anticyclonic and total number of eddies detected by methods A1,

6 B1 and the modified OW.

7

8

9

10

Accepted manuscript

1 Figure Captions

2

3 Figures:

4 Figure 1: Colors indicate the EKE values (units $\text{cm}^2 \text{s}^{-2}$) of sea-level anomalies for the
 5 period 1992–2010 estimated from satellite altimetry data (see text for details of the
 6 dataset). *Black lines* indicate potential vorticity isolines (units $-1 \times 10^{-8} \text{ m}^{-1} \text{ s}^{-1}$) and
 7 range from $-2.1 \times 10^{-8} \text{ m}^{-1} \text{ s}^{-1}$ to $-1.92 \times 10^{-8} \text{ m}^{-1} \text{ s}^{-1}$. The *boldface* closed potential
 8 vorticity contour centred at 43°W, 45°S corresponds to the $-1.92 \times 10^{-8} \text{ m}^{-1} \text{ s}^{-1}$ value
 9 and is used to represent the Zapiola Drift area [Saraceno et al., 2009]. The mean
 10 positions of the Subtropical Front (STF) and the Subantarctic Front (SAF) are from
 11 Saraceno et al. [2004] and are indicated by *black* and *magenta dash-dotted lines*,
 12 respectively. Representative positions of the Brazil Current (BC), Malvinas Current
 13 (MC), Malvinas Return Flow (MRF), Antarctic Circumpolar Current (ACC), South
 14 Atlantic Current (SAC) and overshoot region are indicated.

15

16 Figure 2: **a)** chlorophyll-*a* concentration (mg m^{-3}) in the background; *thin black* and
 17 *red contour lines* are SLA isolines contoured every 10 cm from -100 cm to 0 cm and
 18 from $+10 \text{ cm}$ to $+150 \text{ cm}$; the *blue dotted line* is the trajectory of the buoy # 2529260.
 19 **b)** and **c)** are enlarged regions from **(a)**. *Black (red) circles* correspond to the cyclonic
 20 (anticyclonic) eddies detected by the OW method (*boldfaced-line circles*), method A1
 21 (*dashed-line circle*, see panel **b**) and method B1 (*thin-line circles*). On panel **(b)**,
 22 *black dots* correspond to the part of the buoy trajectory considered to compute the
 23 date of the SLA and chlorophyll-*a* concentration images displayed (27 February
 24 2008). Colorbar on the right refers to the background chlorophyll-*a* concentration
 25 field and is common to the three panels.

26

27 Figure 3: Normalized spatial distribution of the concentration of cyclonic (*panel a*)
 28 and anticyclonic (*panel b*) eddies in the SWA. The total number of eddies whose
 29 centers fall in the area of a given pixel is divided by the largest common value (36).
 30 *Black* and *magenta lines* are as in Figure 1 except for the *boldface black line* which
 31 here corresponds to the $-2.1 \times 10^{-8} \text{ m}^{-1} \text{ s}^{-1}$ potential vorticity contour.. The *red line*
 32 corresponds to the area considered in the count of the number of A and C eddies
 33 inside the ZD.

1

2 Figure 4: Schematic representation of the mechanism proposed to explain the larger
3 number of C (A) eddies inside (outside) the ZD area. *Left panel:* The anticyclonic
4 Zapiola Current (*black arrows*) may generate meanders inside (loop with *blue*
5 *arrows*) and outside the ZD (loop with *red arrows*). *Right panel:* meanders may
6 eventually separate from the main current, creating a C eddy (*blue arrows*) inside the
7 ZD area and an A eddy (*red arrows*) outside the ZD area.

8

9 Figure 5: Potential vorticity contours (units $-1 \times 10^{-8} \text{ m}^{-1} \text{ s}^{-1}$). *Boldface black line*
10 corresponds to the $-1.92 \times 10^{-8} \text{ m}^{-1} \text{ s}^{-1}$ contour.

11

12 Figure 6: Trajectories corresponding to the cyclonic (*panel a*) and anticyclonic (*panel*
13 *b*) eddies detected. SAF and STF are represented by *magenta* and *black dash-dotted*
14 *lines*, respectively. The potential vorticity contour $-1.92 \times 10^{-8} \text{ m}^{-1} \text{ s}^{-1}$ is plotted with a
15 *boldface black line*.

16

17 Figure 7: Number of cyclonic eddies inside the ZD area (*black line*) and a 4-year low-
18 pass-filtered transport time-series associated with the Zapiola Current (*red line*, units
19 Sverdrups, 1 Sverdrup = $10^6 \text{ m}^3 \text{ s}^{-1}$).

20

21 Figure 8: Composite average of chlorophyll-*a* concentration within cyclonic (left
22 panel) and anticyclonic (right panel) eddy interiors in a translating and normalized
23 coordinate system. Only eddies with more than 50% of pixels without clouds have
24 been considered.

25

1 Article's reference number: DSRI 2127

2

3 Title: On eddy polarity distribution in the Southwestern Atlantic

4

5 Authors: Martin Saraceno and Christine Provost

6

7

8 Highlights

9

- 10
- Eddies are detected from 18 years of satellite altimetry data.
 - Eddies are distributed unevenly according to their polarity.
 - Eddies polarity distribution is explained considering direction of the currents.
 - 91% of eddies are cyclonic inside the large Zapiola anticyclone.
 - Chlorophyll-a averaged inside eddies is larger into cyclonic eddies.
- 11
- 12
- 13
- 14
- 15
- 16
- 17
- 18

Accepted manuscript

1 Article's reference number: DSRI 2127

2
3 Title: On eddy polarity distribution in the Southwestern Atlantic

4
5 Authors: Martin Saraceno and Christine Provost

6
7
8 Highlights

- 9
- 10 • Eddies in the Southwestern Atlantic are detected from 18 years of satellite
 - 11 altimetry data.
 - 12 • A larger concentration of cyclonic (anticyclonic) eddies is found on the left
 - 13 (right) side when looking downstream on some of the largest current systems
 - 14 in the region.
 - 15 • The observed distribution of eddies is in agreement with the generation of
 - 16 eddies from meanders of the currents.
 - 17 • In the region isolated by the anticyclonic Zapiola Current, 91% of eddies are
 - 18 cyclonic and enter through the region where the gradient of potential vorticity
 - 19 is lower.
 - 20 • Classical eddy-pumping theory explains the difference in surface chlorophyll-
 - 21 *a* concentration within eddies: average values inside cyclonic eddies are larger
 - 22 than into anticyclonic ones.

23
24 Equations

25
26 (1) $v = \frac{g}{f} \frac{\partial \eta}{\partial x}$

27 (2) $u = -\frac{g}{f} \frac{\partial \eta}{\partial y}$

28 (3) $\omega = v_x - u_y$

29 (4) $S_n = u_x - v_y$

30 (5) $S_s = v_x + u_y$

31 (6) $W = S_n^2 + S_s^2 - \omega^2$

32 (7) $W = 4(v_x u_y + u_x^2)$

33 (8) $D_{e1:e2} = \sqrt{\left(\frac{\diamond D}{D_0}\right)^2 + \left(\frac{\diamond R}{R_0}\right)^2 + \left(\frac{\diamond \mu}{\mu_0}\right)^2 + \left(\frac{\diamond EKE}{EKE_0}\right)^2}$

34
35
36
37

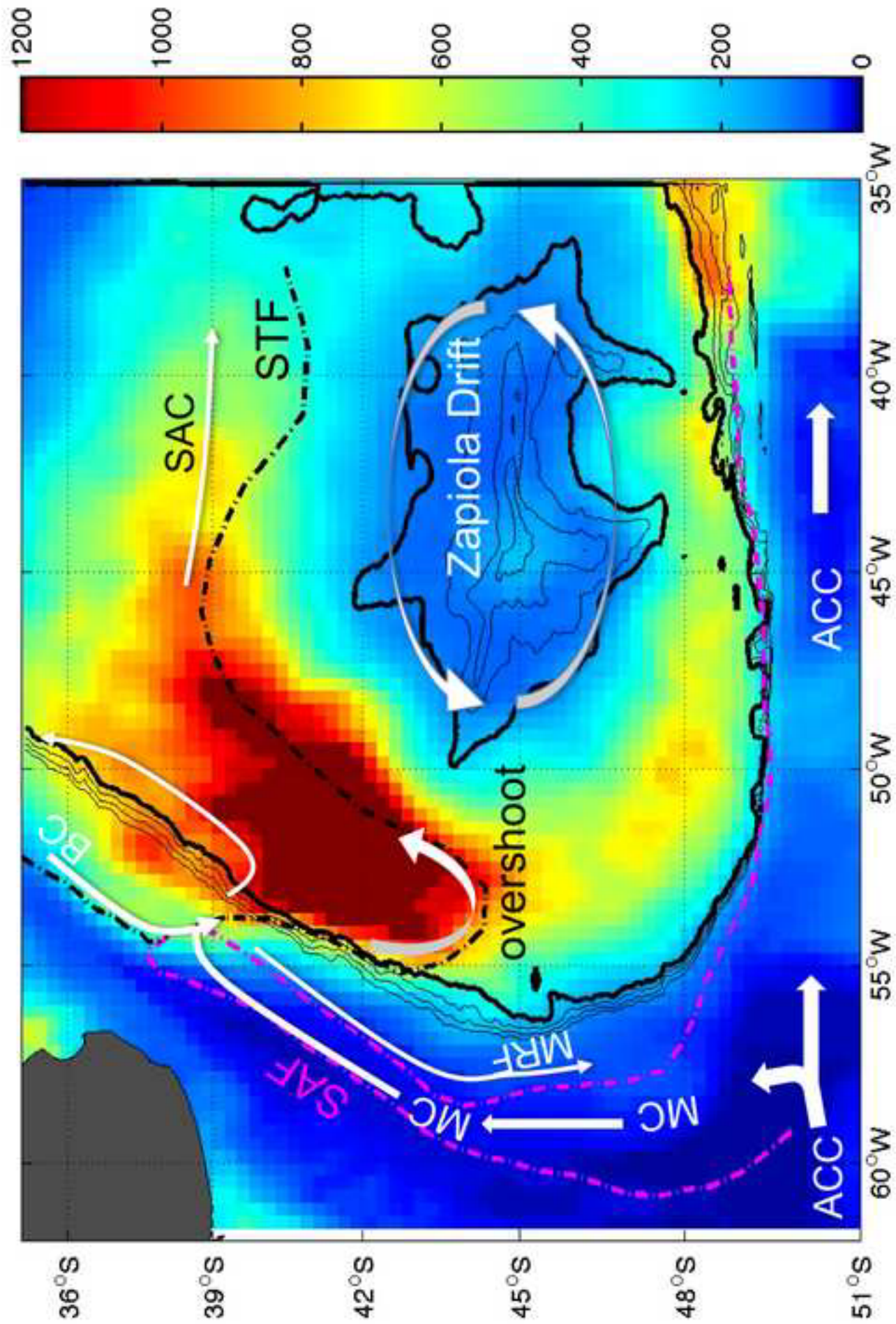


Figure 1

Figure 2

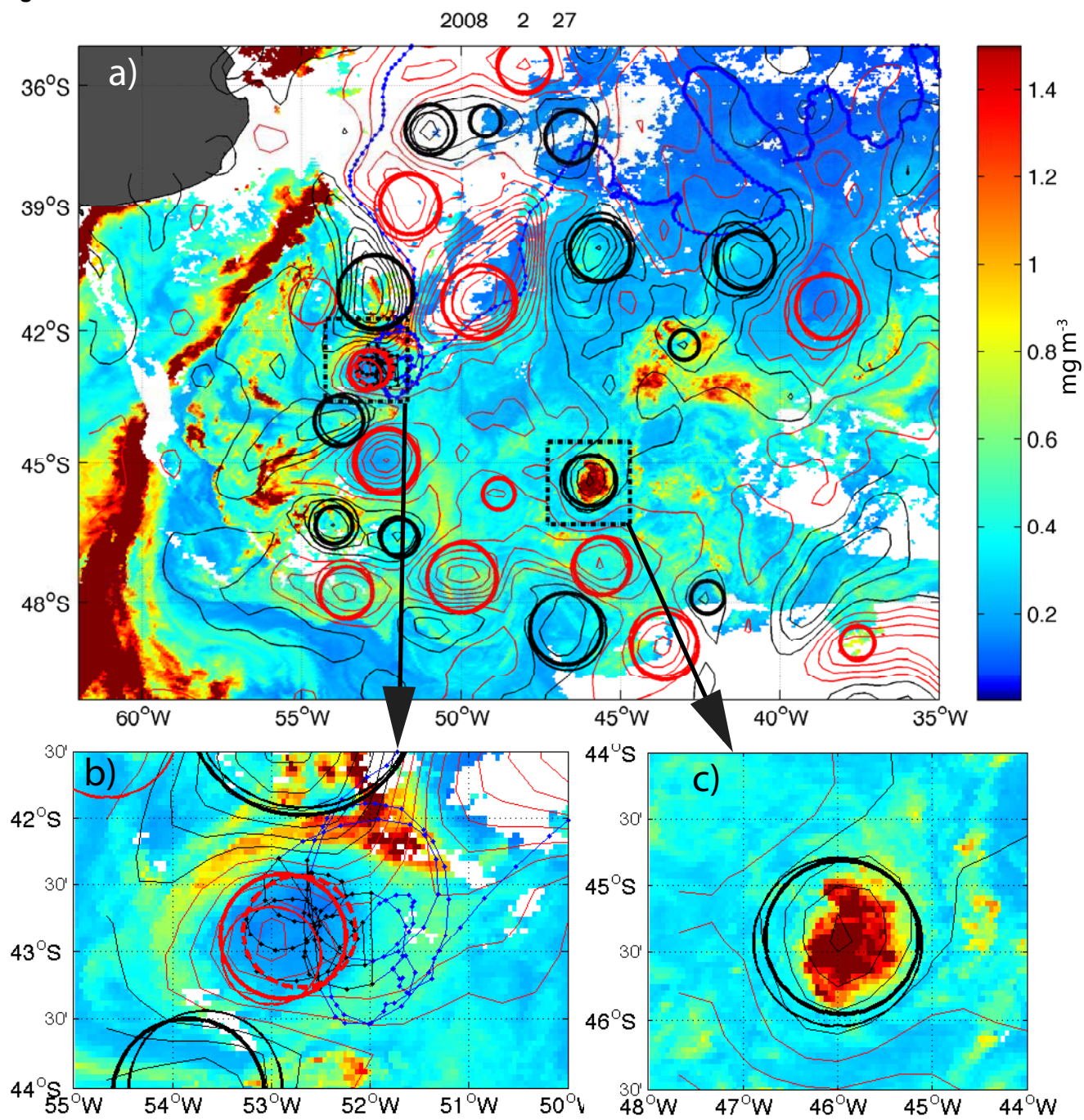
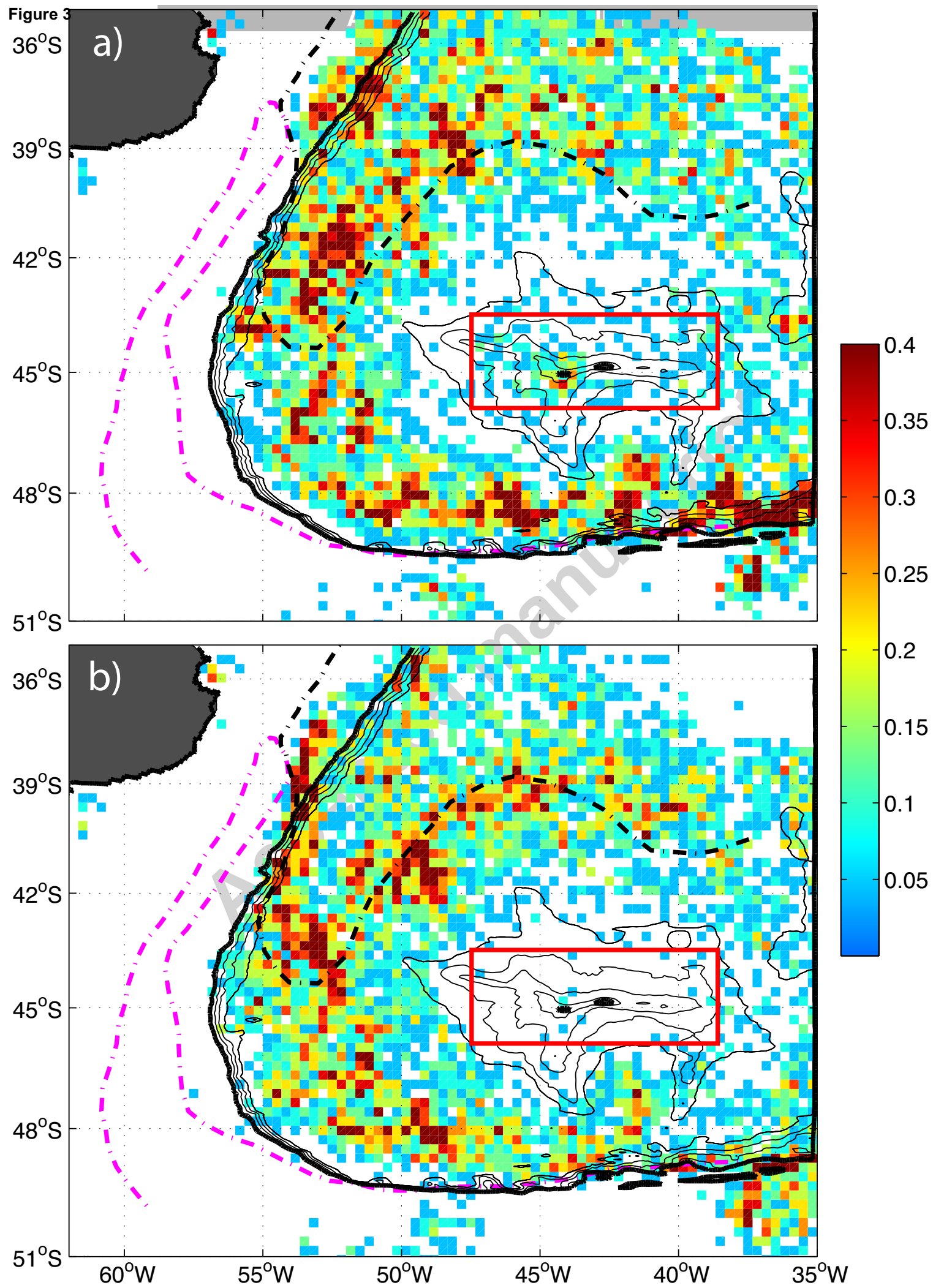
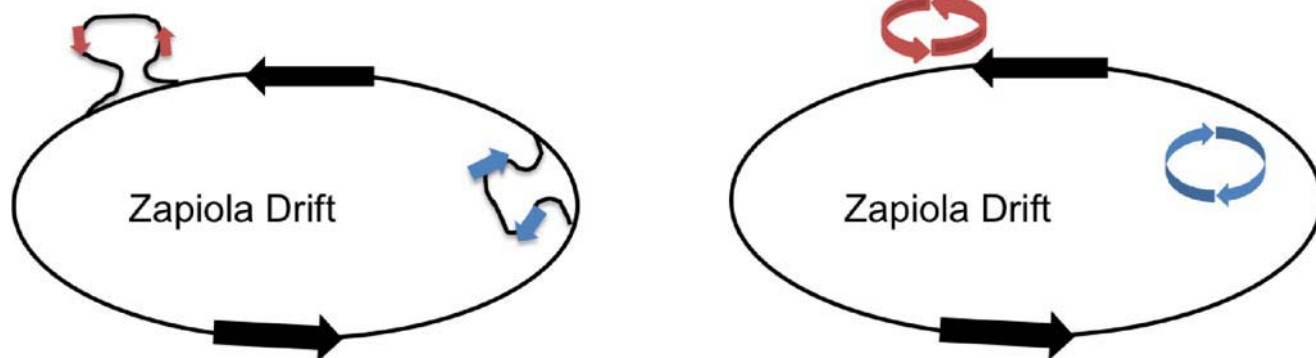


Figure 3





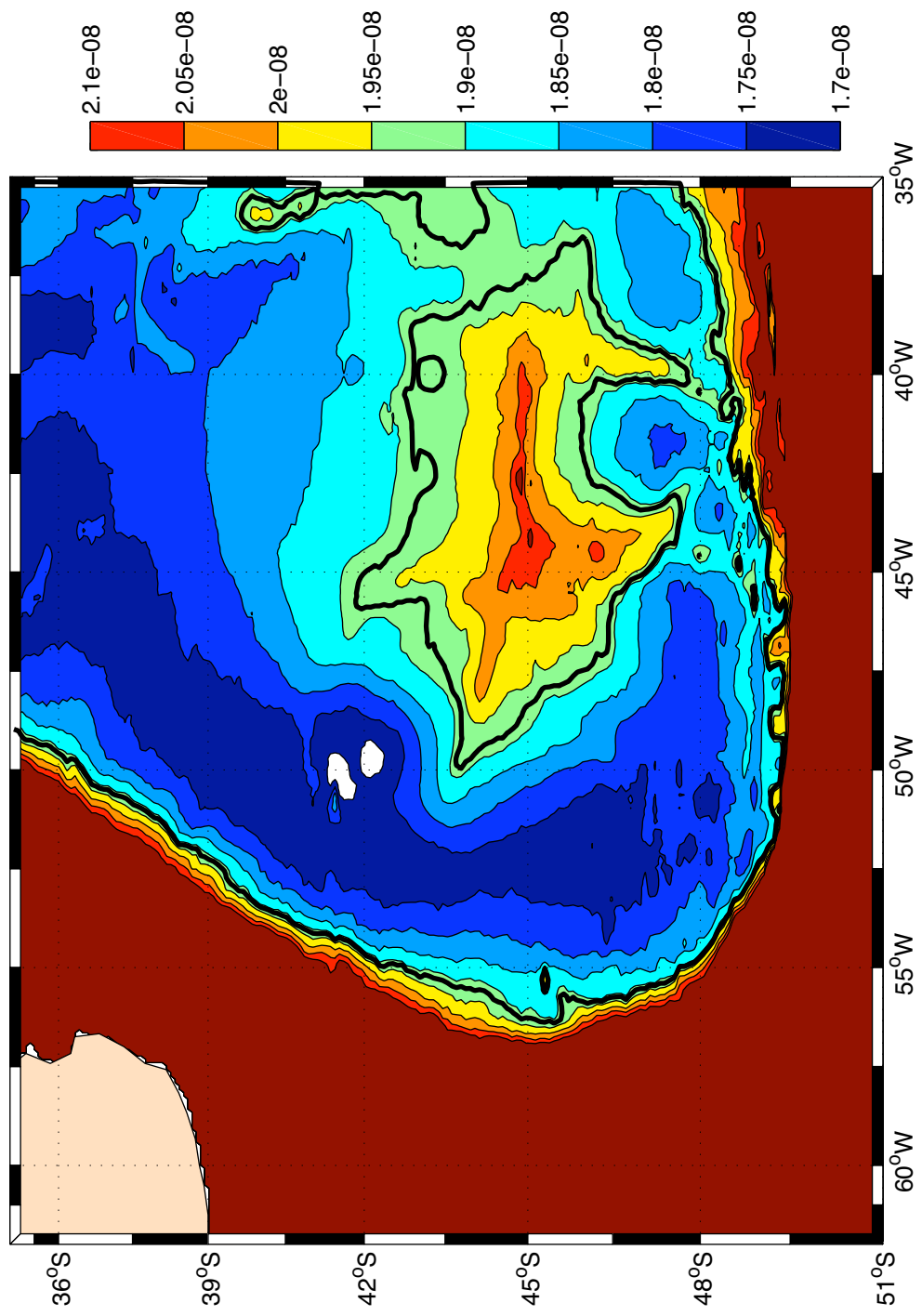


Figure 5

